J Mater Sci (2020) 55:3507–3520

Energy materials

Highly scattered Ir oxides on TiN as an efficient oxygen evolution reaction electrocatalyst in acidic media

Kaikai Zhang[1], Wanshan Mai[1], Jin Li[1], Huan Wang[1], Guoqiang Li[1], and Wei Hu[1,*]

[1] Hubei Collaborative Innovation Center for Advanced Organic Chemical Materials, Ministry of Education Key Laboratory for the Synthesis and Applications of Organic Functional Molecules, Hubei University, Wuhan 430062, China

Received: 7 September 2019
Accepted: 6 November 2019
Published online: 15 November 2019

ABSTRACT

Here, a support-type composite catalyst TiN/IrO_2 with an outstanding catalytic activity for OER in acid electrolyte was prepared by a colloidal method. It was found the ultra-fine IrO_2 nanoclusters (1.41 ± 0.19 nm) scattered on the TiN support like strawberry seeds, which not only provided the higher active surface area, but also exposed much more surface unsaturated Ir atoms with the higher reactive activity compared to saturated iridium atoms. And the mesoporous structure and high surface area inherited from the TiN carrier were also maintained in the composite. Benefit from these characteristics, the as-prepared TiN/IrO_2 with IrO_2 loading of 31 wt% possessed a mass-normalized OER activity of 874.0 A g^{-1}(IrO_2) at the potential of 1.6 V that was about 5.0 times of the unsupported IrO_2 (176.0 A $g^{-1}IrO_2$).

Introduction

As a key link for renewable and sustainable energy storage and conversion process, electrochemical water oxidation has attracted increasing attention due to its advantages of efficiency and cleanliness [1]. Different to the fast hydrogen evolution reaction (HER) on cathode, the oxygen evolution reaction (OER) on anode involving 4-electron transfer is sluggish and has been recognized as a major bottleneck which brings a great anodic overpotential, thus limiting the overall efficiency of water oxidation [2]. Proton exchange membrane (PEM)-based electrochemical water oxidation devices can meet the market-oriented demand of adapting to the varying power inputs of intermittent renewable sources like wind and solar power because of its higher energy efficiency and greater power density compared to alkaline water electrolyzers [3], but they face severe corrosive problems caused by acidic and anodic working environment. As a result, the requirement for efficient, stable, and cost-effective electrocatalysts toward the slow OER in acidic media has become the driving force of current researches on PEM water electrolysis.

Currently, the OER electrocatalysts resistant to acidic media are mainly the expensive and low-reserve Ir- or Ru-based catalysts, in which Ir-based oxides are preferred because of their relative higher stability than other precious Ru-based oxide catalysts

Address correspondence to E-mail: huwei_2013@hotmail.com; 1070323675@qq.com

https://doi.org/10.1007/s10853-019-04201-4

[4–6]. However, the high price and imperfect stability of IrO_x-based catalysts are the main obstacles in the commercialization of the PEM electrolyzer. Since almost no non-noble metal-based OER catalysts are essentially stable in the acid aggressive and strong corrosive conditions, loading Ir metal or oxide nanoparticles on the conductive transition metal oxides has become a feasible strategy for reducing Ir dosage in composites [7–9]. The supported Ir-based composite catalysts are of great advantages of decreasing the overall Ir metal loading and cost of the catalyst and manipulating/controlling dispersion of IrO_x nanoparticles to improve the catalyst utilization and durability. But it remains a great challenge of choosing an appropriate corrosion-resistant support for the Ir-based oxides.

Some widely used conductive carbon support materials, such as carbon blacks or carbon nanotubes, are intrinsically unstable in the anode of PEM electrolyzers because of its highly oxidizing/corrosive environment [10]. Therefore, various acid-resistant and conductive or semi-conductive transition metal oxides or carbides have been applied as alternative supports, such as the doped titanium oxide (Nb-TiO_2), niobium oxide, or tin oxide (ITO and ATO) [7, 11, 12], and have been developed as possible candidates for OER catalyst supports in acidic media. We have prepared $Nb_{0.05}Ti_{0.95}O_2$-supported IrO_2 to catalyze OER in acid, which obtained a higher mass activity (471 A g_{IrO2}^{-1}) and the improved stability than that of the free IrO_2 nanoparticles (198 A $g_{IrO2}{}^{-1}$) at the potential of 1.6 V in our previous works [8]. Strasser et al. have used Sb-doped SnO_2 (ATO) as the support for Ir nanodendrite, and the obtained composite catalyst has exhibited an OER activity (at the overpotential of 280 mV) of 70 A g Ir^{-1} [13]. Moreover, several transition metal carbides (MC) including TaC, WC, NbC, etc., have also been applied as the supports for OER in acid. Karimi et al. [14] have found that Ir/TaC and Ir/WC had an average OER activity (350–400 mA/mg at 1.48 V) compared to other supported catalysts such as Ir/NbC and Ir/TiC. They also summarized that the property importance of the support was in the following order: OER performance ≈ surface area ≫ conductivity. Though above-mentioned supports combined with Ir or IrO_x can provide the initially stable catalyst surface area and also significantly improve the mass activity of the composite catalysts, several major disadvantages have not been overcome including the poor conductivity of metal oxides, the increasing corrosion rate in acidic condition of the Sb doping metal oxides, the low surface area of MC, and its partial oxidation under the high temperature during the preparation process.

Recently, transition metal (i.e. Ti, Fe, Co, Ni) nitrides have gradually developed as the promising carrier materials because of the high conductivity and the low price [3, 15]. Particularly, TiN exhibits expected merits of the metal-like conductivity with a room temperature resistivity of 3.34×10^{-7} (Ω cm) which is higher than that of metal Ti (5×10^{-6}(Ω cm)) and the good acidic/alkaline resistance [16, 17], the excellent oxidation resistance, and the inertia to most chemicals and can be used as a valid electronic structure modulator [18], that might meet all the expectations for a good support. However, most up-to-date works reported in the studies are focused on using TiN as the support for Pt-based catalysts toward the oxygen reduction reaction (ORR), such as Pt-decorated three-dimensional and porous TiN catalyst which possessed much higher catalytic capability for ORR than Pt/C benchmark [19], and a single-atom Pt embellished TiN nanoparticles with unique selectivity and excellent mass activity [20]. It is seldom to probe TiN as the support material toward OER catalysis, except Xing's work which has illustrated IrO_2@Ir/TiN as an OER electrocatalyst with high efficiency [21].

Considering the high temperature during synthesizing procedure may affect the performance of the carrier; herein, we employ a facile and mild colloidal method rather than a common Adams fusion method which needs the temperature at least 500 °C [22] to get the TiN-supported IrO_2 composite catalyst and investigate the OER activity in acidic media. Research shows that TiN plays a very important role in dispersing IrO_2 nanoparticles, and then, the highly scattered IrO_2 on TiN has demonstrated an excellent mass activity for OER. It is also discovered by retrieving the IrO_2 loading-dependent activities of TiN-supported IrO_2 catalysts that the mass activity at 1.6 V on TiN/IrO_2 with the IrO_2 loading of 31 wt% has reached the maximum which is much higher than that of the unsupported IrO_2, meaning it might greatly reduce the precious metal usage via this TiN support strategy.

Experimental section

Synthesis of the TiN-supported IrO_2 nanoparticles

The TiN-supported IrO_2 (TiN/IrO_2) composite was prepared by a protocol modified from Ioroi's work [23, 24], using hexachloroiridic (IV) acid hydrate ($H_2IrCl_6{\cdot}6H_2O$, 47.5 wt%Ir, Shaanxi Kaida Chemical Engineering Co., Ltd.) as the precursor for IrO_2, and the preparation process diagram for TiN/IrO_2 composite catalyst is shown in Fig. 1. Ten milligrams of commercial TiN powders (20 nm, Shanghai Macklin Biochemical Co., Ltd.) was dispersed in 1 mL isopropanol ultrasonically to obtain a black suspension. Then, an appropriate volume of Ir precursor solution which contained a certain dose of $H_2IrCl_6{\cdot}6H_2O$, 4 mL (0.5 mol L^{-1}) NaOH, and 6 mL of deionized water, was added into the TiN suspension and held at 80 °C for 1 h with continuous stirring and N_2 bubbling. After the mixture became dark blue and cool, its pH was reduced to ca. 8 by dropwise addition of 1 mol L^{-1} HNO_3 under stirring for another 30 min. After centrifugation, the black precipitates were separated, washed using distilled water, and dried at 80 °C in vacuum oven for 12 h to obtain some black powders. Finally, these powders were heated at 200 °C for 1 h in air to remove the absorbed water to give TiN/IrO_2 composite, denoted as TiN/IrO_2-x. (Here, x refers to the mass percentage of the loaded IrO_2). By regulating the feed amount of $H_2IrCl_6{\cdot}6H_2O$, TiN/IrO_2-25, TiN/IrO_2-31, TiN/IrO_2-40, and TiN/IrO_2-50 composites were prepared successfully. As the benchmark catalyst, the unsupported IrO_2 powders were also obtained following the similar protocol without TiN support.

Measurement of physical performance

The crystal structure of the obtained samples was measured by X-ray diffraction (XRD, Bruker D8 Advance). Morphology was studied by field emission scanning electron microscopy (FESEM, JEOL, JSM-6700F) and transmission electron microscopy (TEM, JEOL JEM-2010). Surface area and pore size distribution of materials were evaluated via N_2 adsorption/desorption measurements (V-Sorb 2800P, Gold APP Instruments Corporation). Chemical composition analysis was executed through X-ray energy-dispersive spectroscopy equipped on the FESEM. Surface elemental composition and chemical state analysis were conducted by using X-ray photoelectron spectroscopy (XPS, Kratos Ltd., XSAM800). After chronoamperometry (CA) testing for 4 h, elemental analysis of the collected electrolyte (H_2SO_4) was implemented by inductively coupled plasma optical emission spectroscopy (ICP-OES, iCAP 6500 duo, Thermo Fisher) for determining the concentration of Ir and Ti dissolved from the electrocatalysts into the solution.

Test of electrochemical performance

Using a three-electrode system equipped with a rotating glassy carbon electrode (GC, 5 mm, Pine Instrument) as the work electrode, Pt foil as the auxiliary electrode, and a saturated calomel electrode (SCE) as the reference electrode, electrochemical performance of catalysts was tested in 0.5 mol/L H_2SO_4. Before testing, potential of SCE was standardized through measuring the hydrogen evolution and oxidation currents on a Pt disk (Pine) in the H_2-saturated H_2SO_4 electrolyte and taking the voltage at which the current was zero as 0 V versus the reversible hydrogen electrode (RHE). The measured SCE

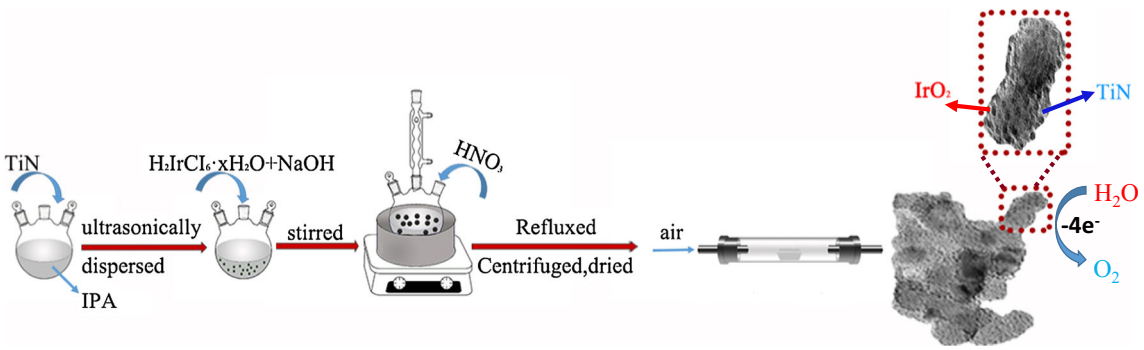

Figure 1 Preparation schematic diagram of the TiN/IrO_2 composite catalyst.

potential versus RHE was 0.27 V, and all the potentials herein were calibrated versus RHE. Electrochemical impedance spectra (EIS) were procured from 100 kHz to 100 mHz at 0.8 V with 10 mV amplitude.

Using ultrasonic machine, a black ink (5 mg mL^{-1}) was obtained by dispersing as-prepared catalyst powders into Nafion-contained isopropanol. Ten microliters of this ink was pipetted onto a GC electrode which was pre-polished using alumina polishing powders (50 nm) and dried in the isopropanol vapor to form a uniform catalyst film. Cyclic voltammograms (CVs) were recorded by scanning from 0.05 V to 1.20 V with a rate of 50 mV s^{-1}. OER linear sweep voltammetry (LSV) measurements were completed in O_2-saturated H_2SO_4 by rotating the GC electrode at 1600 rpm with a scan rate of 10 mV s^{-1}. Electrochemical polish of the catalyst film on GC electrode was conducted before each test which was completed multiple CV cycles at a 500 mV s^{-1} potential scanning rate until obtaining the coincident curves. All electrochemical data on each catalyst were achieved on a CHI660E potentiostat at room temperature and repeated more than four times to ensure the accuracy.

Results and discussion

The comparison of crystal structures of TiN, as-prepared IrO_2, and TiN/IrO_2 nanoparticles is shown in Fig. 2. The diffraction peaks in XRD pattern (Fig. 2a) of TiN nanoparticles, centered at 36.7°, 42.6°, 61.8°, 74.1°, and 77.9°, belong to (111), (200), (220), (311), and (222) planes of TiN (the face-centered cubic structure, PDF#38-1420) [25]. In addition, the broad diffraction peak at 24.6° was also observed, indicating the existence of carbon in the purchased TiN powders. The pattern of the pure IrO_2 prepared following the similar protocol exhibited several faint and broad peaks implying its weak crystallinity because of the low calcination temperature (i.e., 200 °C). It was clearly seen that the characteristic diffraction peaks of TiN/IrO_2-31 sample were fully consistent with the features of the TiN support except for the lower peak intensity which was attributed to the covering or mingled effect of the lowly crystallized IrO_2 on TiN crystal surface. It displayed that the as-prepared TiN/IrO_2 material was a composite of IrO_2 and TiN with a certain amount of carbon. Raman spectra (Fig. 2b) further confirm the existence of carbon in the commercial TiN powders that may be caused by the preparation process. In addition to the response peaks of TiN phase distributed in the wavenumber from 100 to 1000 cm^{-1}, the two characteristic peaks at about 1356 cm^{-1} and 1590 cm^{-1} for D band and G band, respectively, for carbon were visible in the enlarged spectra (inset). And the peak intensity ratio (I_D/I_G), which was usually applied as a parameter to evaluate the crystallization degree of carbon materials, was 0.92 indicating the coexistence of the disordered carbon and ordered carbon.

The catalyst support provides a highly dispersed physical surface for the active component, and thus, excellent porous structure and high surface area are the crucial elements which should be considered for choosing a proper support material, and also the favorable factors for improving the performance of supported composite catalysts. N_2 adsorption–desorption isotherms (Fig. 3a) of TiN, as-prepared TiN/IrO_2-31, and unsupported IrO_2 samples were identified as type IV isotherms with the hysteresis loop located in the relative pressure region of 0.70–0.95, suggesting the existence of mesoporous structures

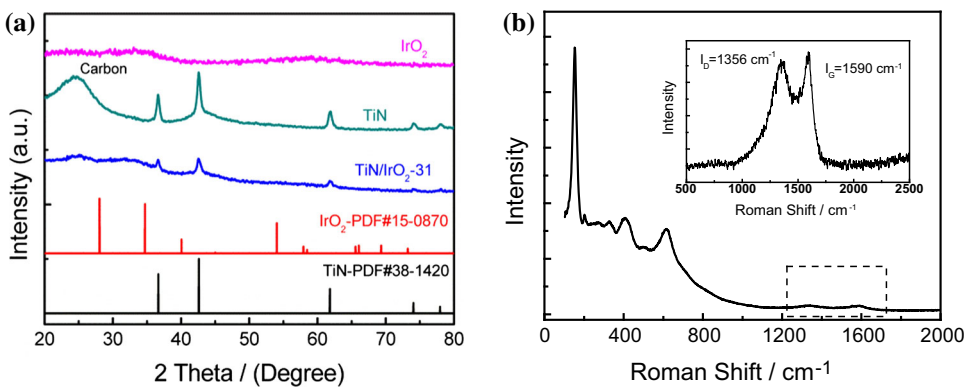

Figure 2 **a** XRD patterns of the TiN, the obtained TiN/IrO_2-31, and unsupported IrO_2 nanoparticles. The straight lines show TiN (PDF#38-1420) and IrO_2 (PDF#15-0870), respectively. **b** Raman spectra of the commercial TiN.

resulted from the stacked holes between the nanoparticles. Besides, BJH pore size distribution analysis based on the desorption branch (Fig. 3b) presented the quite broad pore diameter distributions of three samples ranged from 3 to 450 nm, implying the presence of macropores. Table 1 gives the corresponding physical data comparison for TiN, as-prepared TiN/IrO_2-31, and unsupported IrO_2 samples. In comparison with the unsupported IrO_2 sample, the supported IrO_2 exhibited a relative higher BET surface area, average pore size, and pore volume, which could be attributed to dispersion effect from the TiN carrier.

XPS investigation was conducted to determine the chemical states and the near surface chemical compositions of the Ti, N, and Ir elements in the TiN, TiN/IrO_2-31, and IrO_2 samples (Fig. 4). As depicted in Fig. 4a, Ir 4f (64.3 eV), Ir 4p (495.4 eV), Ti 2p (459.6 eV), Ti 2s (558.2 eV), N 1s (391.3 eV), O 1s (532.4 eV), and C 1s (283.8 eV) were exhibited in the survey spectrum of the obtained TiN/IrO_2-31 composite, confirming the successful loading of IrO_2 on the TiN surface [26, 27]. The high-resolution Ti 2p XPS spectra of TiN with and without IrO_2 loading (Fig. 4b) could be separated into three main peaks with bonding energies of 455.5, 456.8, and 458.4 eV for TiN, and 455.1, 457.5, and 458.5 eV for TiN/IrO_2-31, which were attributed to the Ti–N, Ti–O–N, and Ti–O bonds, respectively [28, 29], meaning that TiN, TiN_xO_y, and TiO_2 species presented on the surface of TiN samples. In Fig. 4c, the N 1s spectra of the two TiN samples were de-convoluted to three peaks at about 396.1, 397.3, and 401.6 eV for TiN, and 395.4, 396.4 and 400.7 eV for TiN/IrO_2-31, which were associated with N–Ti, Ti–O–N, and N–O bonds [29, 30]. These results were consistent with the previous reports which had explained that an oxide layer had formed when TiN was exposed to air [31, 32]. Figure 4d compares Ir 4f XPS spectra of IrO_2 and TiN/IrO_2-31, which were de-convoluted to Ir^{4+} (61.9 eV) and Ir^{3+} (62.2 eV) for TiN/IrO_2, and Ir^{4+} (61.7 eV) and Ir^{3+} (62.2 eV) for IrO_2, respectively, with an Ir 4f doublet splitting energy of 3 eV, matching well with the reported XPS results of the commercial IrO_2 and Li-IrO_2 [33, 34]. The molar ratio between Ir^{4+} and Ir^{3+} evaluated from the corresponding peak area was 1.9:1 for TiN/IrO_2-31, slightly higher than that of the pure IrO_2 (Ir^{4+}/Ir^{3+} was 1.4:1), suggesting that the Ir^{4+} species on the surface of TiN/IrO_2-31 were at the majority. This subtle difference was because the TiN carrier gained the electrons from the active component which would improve the adsorption of oxygen-containing intermediates to accelerate OER, reflecting the strong metal–support interaction (SMSI effect) between TiN and IrO_2. Because the binding energy of oxygen species on the metal oxide surface can reflect their interaction with metal cations, the comparison of O 1s spectra of IrO_2 and TiN/IrO_2-31 is further shown in Fig. 4e, which were decomposed into three peaks, the lattice oxygen ($O_{Ir\text{-}O}$ or $O_{Ti\text{-}O}$) at 530.0 eV for TiN/IrO_2-31 and 529.9 eV for IrO_2, the coordinatively unsaturated oxygen or oxygen in hydroxyl group (O_{OH}) at 531.7 eV for TiN/IrO_2 and 531.5 eV for IrO_2, and the oxygen in adsorbed water (O_{H2O}) at 533.0 eV for TiN/IrO_2 and 533.1 eV for IrO_2, respectively. And the peak area percentage sum of O_{H2O} and O_{OH} in IrO_2 was 81.7%, while the data in TiN/IrO_2 were 93.8%, meaning the surface O_{OH} and O_{H2O} was dominant. It indicated that oxygen species which interacted with Ir weakly on the TiN/IrO_2 surface exhibited a relative higher ratio than that of IrO_2. Though underlying reasons were unknown, it had been observed that hydrated or hydroxylated amorphous iridium oxides generally possess higher activity toward OER than the excellent crystalline

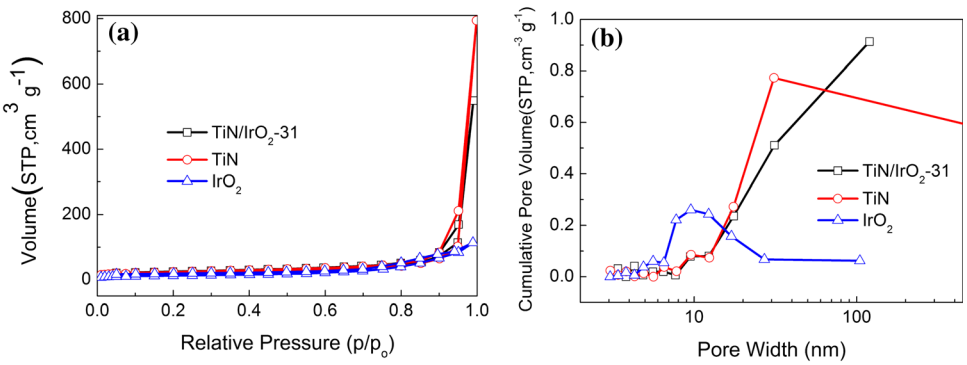

Figure 3 **a** N_2 adsorption–desorption isotherms and **b** pore width distributions corresponding to the desorption branch of the TiN, as-prepared TiN/IrO_2-31, and unsupported IrO_2 nanoparticles.

Table 1 Physical data of the TiN, as-prepared TiN/IrO_2-31, and unsupported IrO_2 samples

Sample	Samples particle size in XRD (nm)	BET surface area (m^2 g^{-1})	Average pore size (nm)	Pore volume (cm^3 g^{-1})
TiN	9.6	68.8	15.5	1.215
IrO_2	–	47.2	3.9	0.168
TiN/IrO_2-31	8.3	65.5	15.6	0.838

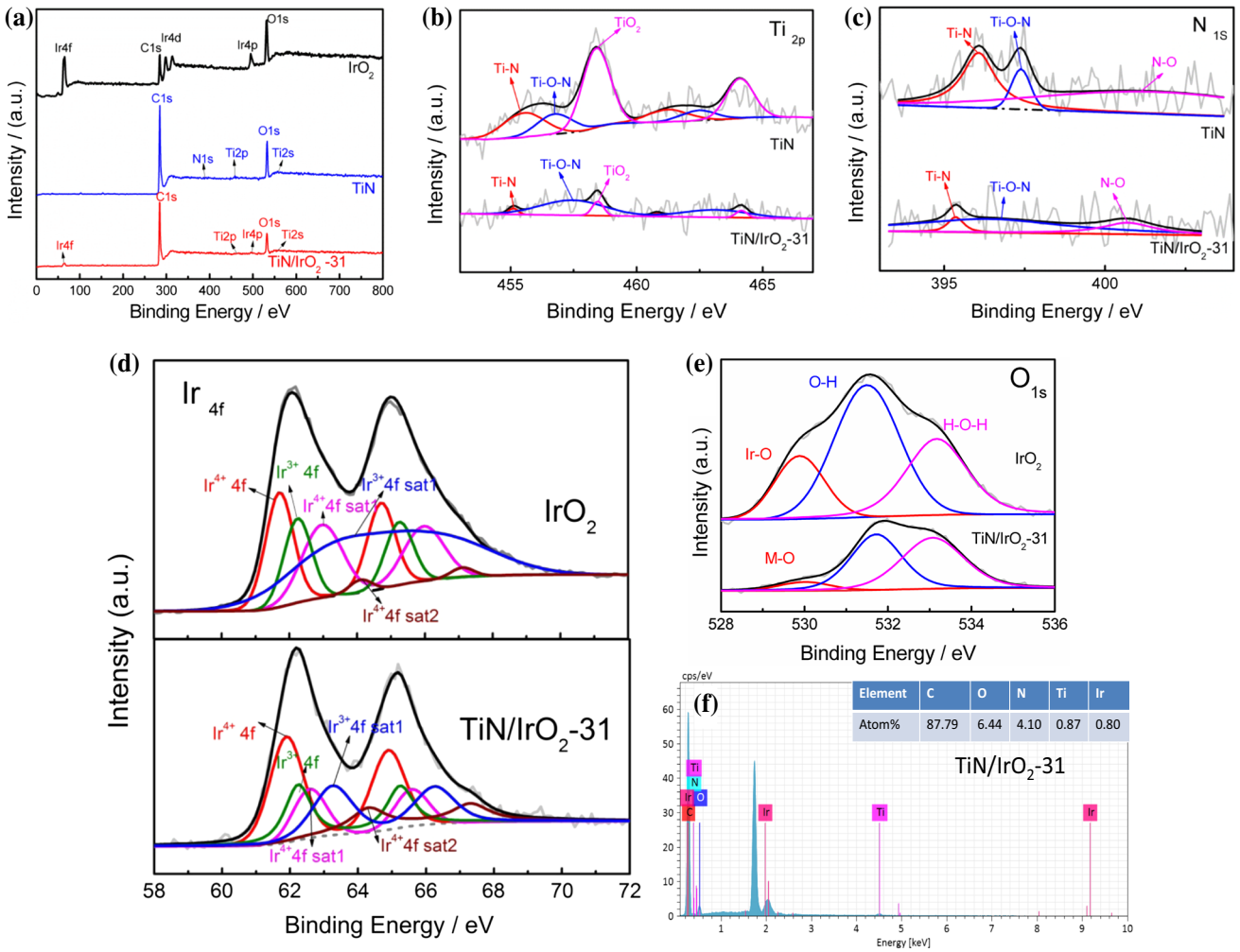

Figure 4 XPS results of the TiN, as-obtained TiN/IrO_2-31, and unsupported IrO_2 samples. **a** XPS survey spectrum of three samples. **b** High-resolution Ti 2p spectra of TiN and TiN/IrO_2-31. **c** High-resolution N 1s spectra of TiN and TiN/IrO_2-31. **d** High-resolution Ir 4f spectra of the free and loaded IrO_2. **e** High-resolution O 1s spectra of IrO_2 and TiN/IrO_2-31. **f** EDX chemical composition of TiN/IrO_2-31.

IrO_2 [34, 35]. It can also be used as an explanation for the high OER activity observed on TiN/IrO_2. Both TiN/IrO_2 and IrO_2 samples had a big O_{OH} peak percentage showing that there existed more O species which relatively weakly bonded with metal cations (M) than that in the rutile IrO_2 prepared under a higher temperature, and it was similar to the results observed on the surface of amorphous Li-IrO_2 [35]. Here, TiN/IrO_2 and IrO_2 were heat treated at only 200 °C, significantly lower than most commonly temperatures used in the literature, which was why such high proportion of weakly bound oxygen exists. In addition, chemical composition in TiN/IrO_2-31 sample was also investigated by EDX (Fig. 4f)

showing the molar ratio of Ti/N/Ir was 1:4.7:0.92, which was different from the XPS result (1:5.8:2.3), proving Ir preferentially distributed on the surface of the composite.

FESEM images revealed (Fig. 5a, b) that TiN/IrO_2-31 sample exhibited the similar spherical morphology with TiN, but a slightly larger particle size (50.9 ± 7.8 nm) than the TiN nanoparticles (47.6 ± 5.2 nm). TEM was applied for the further observation of the differences between two samples. Before loading the IrO_2, TiN was composed of random-shaped nanospheres (Fig. 6a), consistent with its SEM results. And the high-resolution TEM (HRTEM) image of the nanocrystals (Fig. 6b) showed a clear crystal face structure with a lattice spacing of ca. 0.21 nm, belonging to the TiN (200) plane (PDF#38-1420) with the diffraction rings and spots seen from its selected area electron diffraction (SAED) image (Fig. 6c). However, after loading with IrO_2, TiN was decorated by plenty of scattered IrO_2 dots with the size of 1.41 ± 0.19 nm (Fig. 6d). HRTEM images displayed strawberry-shaped balls (see Fig. 6e) with diffuse rings (Fig. 6f) because of the influence from the weak crystallinity of IrO_2, consistent with the XRD results. The TEM results were significantly different from the reported wrapped topography of the $Nb_{0.05}Ti_{0.95}O_2/IrO_2$ [8] and meso-Sb-SnO_2/IrO_2 [9], which would be one of the reasons for the surpassing performance on TiN/IrO_2 for OER.

IrO_2 loading-dependent electrochemical activities for TiN-supported IrO_2 catalysts were analyzed in details. For investigating the change in surface Ir oxide, the CVs from the first to the third cycle are recorded and shown in Fig. 7 by taking TiN/IrO_2-31, TiN/IrO_2-40, and unsupported IrO_2 as examples. Unlike IrO_2@Ir/TiN catalysts reported by Xing [21], almost no obvious H underpotential deposition peak

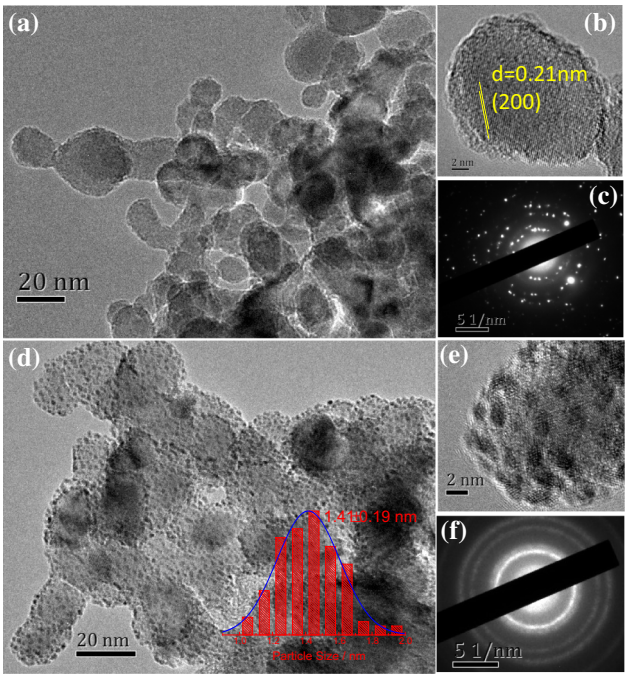

Figure 6 TEM images of TiN and TiN/IrO_2-31 samples. TEM (**a**), HRTEM (**b**), and SAED (**c**) images of TiN support. TEM (**d**), HRTEM (**e**) and SAED (**f**) images of TiN/IrO_2-31 composite. Inset in (**d**) was particle size distribution of the loaded IrO_2 nanoparticles.

(located at 0–0.4 V), which was the confirmation of Ir metal existence, appeared in the first cycle in CVs, and no significant changes arose in CVs for the initial reactive surface and the surface after several potential cycles. It meant that Ir in these composites presented mainly in its oxidation state, consistent with the previous XPS results. While compared with the CVs of the unsupported IrO_2, the weak peaks located at 0.05–0.3 V in CVs for TiN/IrO_2 still could be observed, due to the influence of the TiN carrier. To further analyze the interaction between the carrier

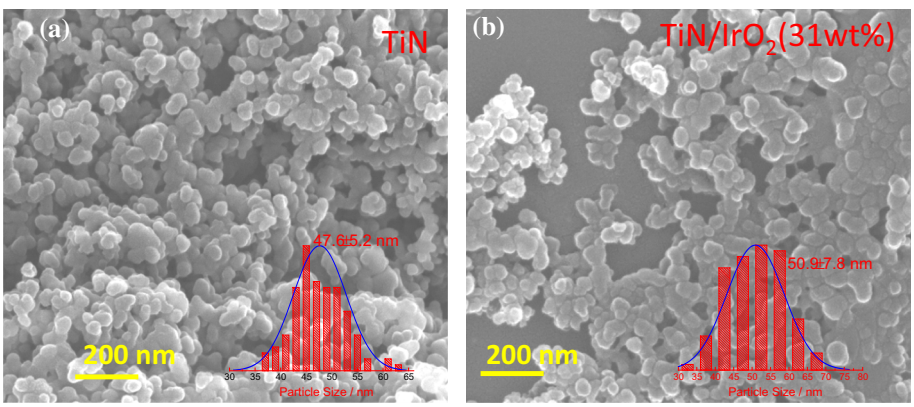

Figure 5 FESEM images of TiN (**a**) and TiN/IrO_2-31 (**b**). Insets were the corresponding particle size distribution.

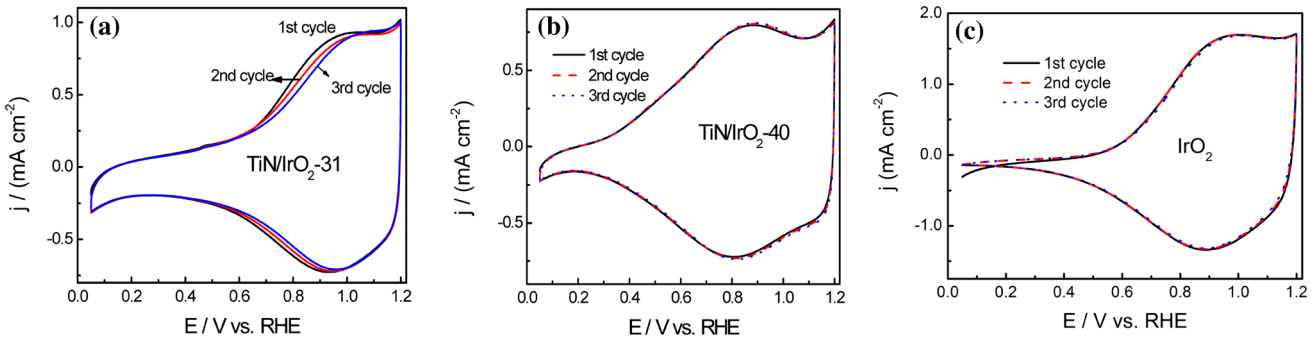

Figure 7 Cyclic voltammetry curves of **a** TiN/IrO_2-31, **b** TiN/IrO_2-40, and **c** unsupported IrO_2 recorded between 0.05–1.2 V potential window at 50 mV s^{-1} in Ar-saturated 0.5 mol L^{-1} H_2SO_4 with the catalyst loading of 0.255 mg cm^{-2}.

and the active ingredient, Fig. 8a gives the representative CVs of TiN/IrO_2-25, TiN/IrO_2-31, TiN/IrO_2-40, TiN/IrO_2-50 composite catalysts, the unsupported IrO_2, and the TiN support. All the TiN-supported IrO_2 catalysts presented the typical pseudocapacitor features similar to the pure IrO_2 with the redox peaks at about 0.8–1.0 V corresponding to the conversion between different Ir valence states (III^+/IV^+) [5, 36, 37], which were analogous to the surface electroadsorption/desorption. Based on the CV charge (q) via integrating the voltammograms from 0.3 to 1.25 V which were recorded at a potential scanning rate of 50 mV s^{-1}, the electrochemical active surface areas (ECSAs) can be estimated by using an ECSA-charge constant of 1681 cm^2 C^{-1} [38] and are given in Fig. 8b. It was displayed that the TiN/IrO_2-31 and -40 composites had relative higher ECSA (6.3 cm^2 and 6.7 cm^2, respectively) than other TiN/IrO_2 catalysts, but it was still less than the value recorded on the pure IrO_2 (11.8 cm^2). A distinct enhancement in ECSA signified the increase in the accessible of active surface of Ir content, meaning that ECSA was related to the accessible active site numbers, rather than the Ir content alone [39]. So, in the cases with too high IrO_2 loading (i.e., TiN/IrO_2-50), some inner surfaces of IrO_2 cannot be fully utilized because they cannot be accessed by the electrolyte easily, and thus, its ECSA value was less than that of the TiN/IrO_2-31 and -40 samples, which possessed the relative lower Ir dosage. Furthermore, the TiN/IrO_2 composites showed different IrO_2 mass-normalized ECSAs, and the TiN/IrO_2-31 catalyst marked the maximum (406.1 cm^2 mg_{IrO2}^{-1} or 281.8 C g_{Ir}^{-1} with respect to the metal mass), which was almost 1.7 times of the unsupported IrO_2 (236.0 cm^2 mg_{IrO2}^{-1}) and much higher than the results reported on the porous Ir-ND (108.2 C g^{-1}Ir), Ir black (63.7 C g^{-1}Ir) [13], and Nb-TiO_2-supported IrO_2 (40%) (142.0 C g_{Ir}^{-1}) [40]. Above results clearly demonstrated that TiN exhibited a wonderful dispersion effect as the support for IrO_2, where small particle sizes (1.41 ± 0.19 nm) and

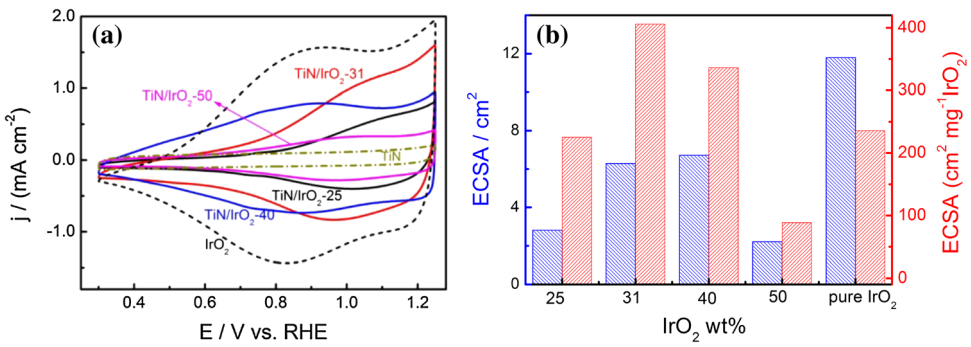

Figure 8 Typical CVs of TiN/IrO_2 composites with different IrO_2 dosages (**a**), and the IrO_2 loading-dependent ECSAs of the supported and pure IrO_2, the relationship between the IrO_2 wt% in the composites and the mass-normalized ECSAs (**b**). The coated catalyst on the glass carbon electrode was 0.255 mg cm^{-2}. The current density (j) in (**a**) was normalized to the geometric area of GC RDE (0.196 cm^2), while ECSA (right) in (**b**) was normalized to the IrO_2 mass.

highly dispersed IrO_2 leaded to higher Ir atomic utilization efficiency.

OER catalytic performance of these catalysts was evaluated by polarization test in O_2-saturated H_2SO_4 solution and at the electrode rotation rate of 1600 rpm. For TiN/IrO_2-25 and 50, in spite of the dispersion role coming from the support, relative lower ECSA made them unable to afford enough active sites to drive OER, so their performance was inferior to the unsupported counterpart, the pure IrO_2. By contrast, TiN/IrO_2-31 possessed prominent activity among those mentioned catalysts, even better than the benchmark IrO_2 catalyst (Fig. 9a), which might be expounded by the electronic modulation of Ir because of the introduction of TiN carrier and its highest mass-normalized ECSA. The comparison of potential (E) at 10 mA cm^{-2} and 40 mA cm^{-2} on these catalysts is shown in Fig. 9b, showing in spite of the slightly higher overpotential at 10 mA cm^{-2} than that of the unsupported counterpart, and the smallest overpotential at 40 mA cm^{-2} was recorded on TiN/IrO_2-31 (Fig. 9b). It meant TiN/IrO_2-31 had superior catalytic activity at high potential region. The corresponding IrO_2 mass-normalized LSV curves clearly demonstrated the superiority of TiN/IrO_2 composites relative to the unsupported counterpart and TiN/IrO_2-31, exhibiting the highest IrO_2 mass-normalized current value (Fig. 9c). Excitingly, the mass activity at 1.6 V of TiN/IrO_2-31 reached 874.0 A g_{IrO2}^{-1}, which was 5.0 times as high as that of the unsupported IrO_2 (176.0 A g_{IrO2}^{-1}) and higher than the results on $Nb_{0.05}Ti_{0.95}O_2/IrO_2$ (471 A g_{IrO2}^{-1}) [8] and meso-Sb-SnO_2/IrO_2 (394 A g_{IrO2}^{-1}) [9]. Obviously, the addition of TiN support enhanced the catalytic efficiency of the active component in these composite catalysts. We further compare the OER activity of TiN/IrO_2-31 with those of recently reported and representative iridium-based electrocatalysts (Table 2) by listing their overpotential at 10 mA cm^{-2} and mass specific activity. The comparison indicated that TiN/IrO_2-31 was among the most outstanding Ir-based electrocatalysts for OER under acidic conditions, although there might be some differences in catalytic testing methods, catalyst loading, and acidic concentration adopted by different researchers. The area-normalized activity comparison was implemented on the ECSAs (Fig. 9d), indicating that TiN/IrO_2-31 composite possessed the maximum ECSA specific activity (2.7 A cm^{-2}), which was 3.5 times of the result on IrO_2 (0.8 A cm^{-2}). The boosted OER activity

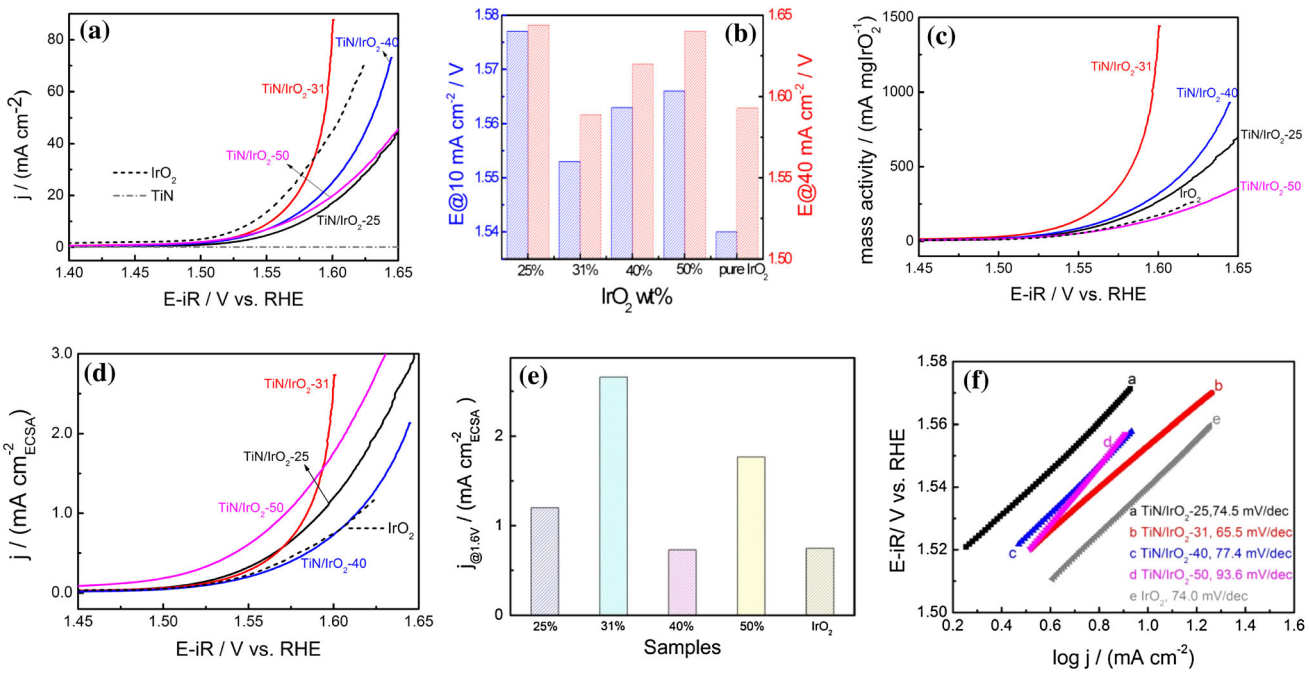

Figure 9 Electrocatalytic oxygen evolution reaction (OER) activities of TiN/IrO_2 composite catalysts with different IrO_2 loadings and the homemade pure IrO_2. **a** LSV curves after iR correction at the scanning rate of 10 mV s^{-1}. **b** The detailed comparison of potential at current density of 10 mA cm^{-2} and 40 mA cm^{-2}, respectively. **c** IrO_2 mass-based LSV curves. **d** Specific activity LSV curves based on the ECSA. **e** Area specific activity comparison at 1.6 V. **f** The corresponding Tafel plots.

Table 2 Comparison of the OER overpotential and mass specific activity for TiN/IrO_2-31 with the Ir-based materials reported to date that were tested in acidic conditions

Catalysts	Loading on GC (mg cm^{-2})	Electrolyte	Scanning rate (mV s^{-1})	Overpotential at 10 mA cm^{-2} (mV vs. RHE)	Mass specific activity at 1.6 V	Refs.
TiN/IrO_2-31	0.255	0.5 M H_2SO_4	10	313	874.0 A g_{IrO2}^{-1}	This work
IrO_2@Ir/TiN (60 wt%)	0.379	0.5 M H_2SO_4	5	265	480.4 A g_{Ir}^{-1}	[21]
IrO_2/$Nb_{0.05}Ti_{0.95}O_2$ (33 wt%)	0.255	0.5 M H_2SO_4	5	239	476.8 A g_{IrO2}^{-1}	[8]
IrO_2/meso-Sb-SnO_2 (31 wt%)	0.102	0.5 M H_2SO_4	5	386	216.1 A g_{IrO2}^{-1}	[9]
Ir/TiC	0.122	0.1 M $HClO_4$	10	>320 versus SHE	150@1.55 V A g_{Ir}^{-1}	[46]
Ir-ND/ATO	0.0102_{Ir}	0.05 M H_2SO_4	5	~400	135.8 A g_{Ir}^{-1}	[13]
IrO_2-Ir	0.133_{Ir}	0.5 M H_2SO_4	5	300	175@1.55 V A g_{Ir}^{-1}	[39]
Ir black	0.133_{Ir}	0.5 M H_2SO_4	5	333	60@1.55 V A g_{Ir}^{-1}	[39]
NiIr-200-CL	0.0117_{Ir}	0.1 M $HClO_4$	20	–	1000@1.55 V A g_{Ir}^{-1}	[47]
NiIr-300-CL	0.0091_{Ir}	0.1 M $HClO_4$	20	–	650@1.55 V A g_{Ir}^{-1}	[47]
$IrCo_{0.65}$ NDs	0.09	0.1 M $HClO_4$	5	281	~533@1.55 V A g_{Ir}^{-1}	[48]
5.9 wt% Ir/g-C_3N_4/NG	0.0067	0.5 M H_2SO_4	5	287	2310 A g_{Ir}^{-1}	[49]
IrO_2/CNT	–	0.5 M H_2SO_4	5	293	–	[43]
$IrNiO_x$/meso-ATO	0.0102_{Ir}	0.05 M H_2SO_4	5	330	~89.8 A g_{Ir}^{-1}	[50]
Ir-STO	~0.21	0.1 M $HClO_4$	1	247	820@1.525 V A g_{Ir}^{-1}	[51]
Li-IrO_x	0.125	0.5 M H_2SO_4	1	290	100@1.525 V A g_{Ir}^{-1}	[34]

corresponded to the electronic structure modulation of Ir by adding TiN [21]. However, for the supported catalysts containing high Ir dosages, such as TiN/IrO_2-40 and TiN/IrO_2-50, the specific activity was lower than that of TiN/IrO_2-31 and pure IrO_2 (Fig. 9e), and the reason was mainly the invalid application of the inner precious metals. Tafel plots of all the TiN/IrO_2 and IrO_2 catalysts were fitted from their corresponding LSV curves to study the reaction kinetics (Fig. 9f). It was shown that TiN/IrO_2-31 gave the smallest Tafel slope (65.5 mV dec^{-1}) among all the investigated samples, revealing the most favorable reactive kinetics toward OER.

Based on the above analysis, we thought that the significantly boosted OER activity of the TiN/IrO_2-31 catalyst mainly benefitted from the following factors: (1) the favorable morphology and size of the IrO_2 nanoclusters which homogeneously dispersed on the conductive TiN surface, (2) the superior conductivity of TiN carrier compared with other oxides (such as the nonstoichiometric TiO_2, transition metal doped TiO_2, or SnO_2), which favored the electrical conduction efficiency during the OER process [20, 41, 42], and (3) the electronic modulation of Ir from the TiN support. Among them, highly scattered nanoclusters contributed the most to enhance activity. It was

interesting to see that IrO_2 clusters with the size of only about 1.4 nm spread like strawberry seeds on the surface of the carrier, completely different from the cladding structures obtained in our previous work (i.e., $IrO_2/Nb_{0.05}Ti_{0.95}O_2$ and IrO_2/meso-Sb-SnO_2). It had already been demonstrated the structure sensitivity of OER over IrO_2 experimentally and theoretically, and the decrease in its particle size did have a beneficial influence on OER activity [43]. Specifically, compared with the unsupported IrO_2, the supported IrO_2 on the TiN carrier with the size less than 2 nm would not only afford much more reactive sites, but also expose much more surface unsaturated Ir atoms. It was illustrated that the surface unsaturated iridium atoms reacted more easily with water to form surface –OH groups because of their larger water-binding energy compared to the saturated iridium atoms [34, 44, 45].

The electrochemical stability of the as-obtained TiN/IrO_2-31 catalyst was also investigated together with the unsupported IrO_2 as the reference sample through chronopotentiometry (CP) and chronoamperometry (CA) measurements at 1600 rpm rotation rate in O_2-saturated 0.5 M H_2SO_4 medium (Fig. 10). CP results (Fig. 10a) showed that the potential rise occurred within 40 min of the test for both IrO_2 reference and TiN/IrO_2-31 sample, after that the potential on IrO_2 became gradually stable, but the potential of TIN/IrO_2-31 was still increasing. Similar results also appeared in CA test (Fig. 10b) which was shown up more clearly than that in CP, because the current was exponential with the potential [52]. After testing for about 40 min, the current on IrO_2 held constant, while the current during the 4-h test on TiN/IrO_2-31 experienced a three-step process of sharp (0–40 min), slow (40–100 min), and rapid (> 100 min) declines. The deactivation rate (the slope of curves) in the first step of TiN/IrO_2 was slightly slower than that of IrO_2, meaning that the corrosion of the supported IrO_2 might be the dominant reason in this case and TiN support delayed this process to some extent. The subsequent activity degradation in the second and third steps was possibly due to the oxidative corrosion of carbon contained in the commercial TiN support, the decrease in conductivity caused by local oxidation of TiN, and the dissolution or detaching of the highly scattered IrO_2 nanoclusters on the outer surface of the catalyst film. Meanwhile, the comparison of CV curves before and after 4 h of continuous operation (Fig. 10c) displayed obvious reduction in redox peak area for TiN/IrO_2, suggesting the loss of surface active sites. Furthermore, ICP analysis conducted in the 0.5 mol L^{-1} H_2SO_4 electrolyte which was collected after CA measurement for 4 h showed that almost no Ti was leached out from the support (its concentration was below the detection limit) suggesting the chemical stability of the TiN carrier. However, H_2SO_4 solution after 4 h of CA for the unsupported IrO_2 and TiN/IrO_2-31 was contained 0.006 ppm and 0.069 ppm of Ir, respectively, which proved that the relatively significant drop in current on TiN/IrO_2-31 was mainly because of the dissolution of outer layer Ir atoms on the tiny nanoclusters. TEM observation on both bare TiN and TiN/IrO_2-31 after continuous electrolysis for 4 h also found that TiN after stability test exhibited no significant morphology changes (Fig. 11a), while for the electrolyzed TiN/IrO_2 composite, some IrO_2 nanoparticles were stripped from the TiN supports (Fig. 11b) which was one of the reasons for the huge changes in OER activity. It could be clear that the tiny and highly scattered IrO_2 nanoclusters actually exercised like a double-edged sword which possessed the high activity for OER but unsatisfactory

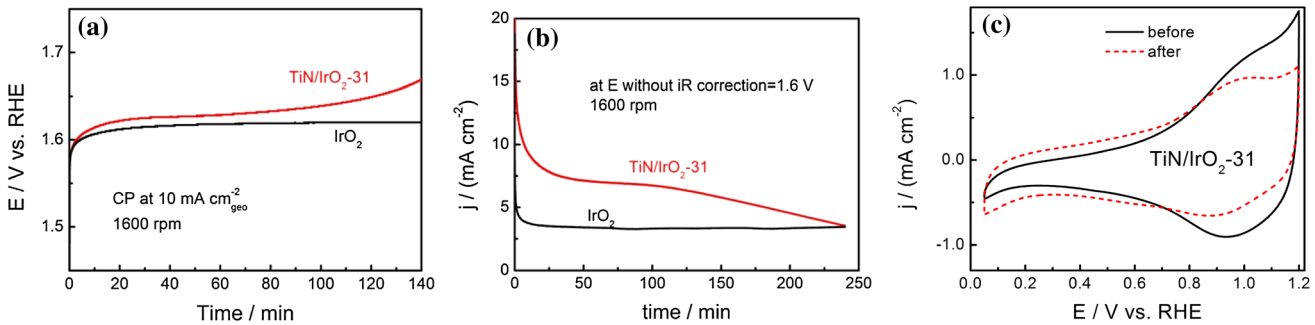

Figure 10 Chronopotentiometry (**a**) and chronoamperometry (**b**) tests on TiN/IrO_2-31 and pure IrO_2 performed in 0.5 mol L^{-1} H_2SO_4 and at 1600 rpm. **c** CVs comparison of TiN/IrO_2-31 before and after CA test at 1.6 V.

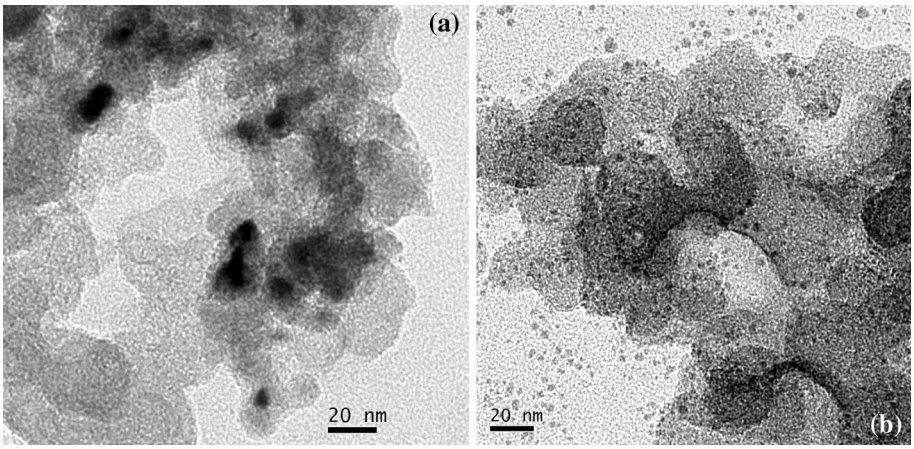

Figure 11 TEM images of the bare TiN (**a**) and TiN/IrO_2-31 (**b**) after 4-h chronoamperometry test.

stability during the continuous polarization. Our further work should be concentrated on the balance between activity and durability of these superfine IrO_2 clusters.

Conclusions

In conclusion, we had constructed a TiN-supported IrO_2 composite electrocatalyst for OER in acidic media based on a novel catalyst/support couple strategy to boost the utilization efficiency of the noble metal. The optimized TiN/IrO_2 sample had mesoporous structure with the high surface area sourced from the TiN support, which enabled the dispersion of the active ultra-small nanoclusters. Moreover, a strong active component–support interaction between TiN and IrO_2 urged the TiN carrier to gain the electrons from the active component, thus benefiting OER. With the IrO_2 loading of 31%, TiN/IrO_2 catalyst possessed an excellent mass-normalized ECSA and the outstanding OER activity. TiN support not only provided high conductive substrate for the catalyst, but also promoted the high dispersion for noble metals, so that precious metals can be used efficiently. This development of ultra-fine iridium oxide as highly efficient OER electrocatalyst greatly promoted the utilization of precious metals and demonstrated a good prospect for the practical application. However, obtaining the satisfactory stability on those highly dispersed Ir-based nanoclusters was still a challenge.

Acknowledgements

This work was supported by the National Natural Science Foundation of China (NSFC No. 21606075).

References

[1] Sun W, Zhou Z, Zaman WQ, Cao L, Yang J (2017) Rational manipulation of IrO_2 lattice strain on α-MnO_2 nanorods as a highly efficient water-splitting catalyst. ACS Appl Mater Interfaces 9(48):41855–41862

[2] Tariq M, Zaman WQ, Sun W, Zhou Z, Wu Y, Cao L, Yang J (2018) Unraveling the beneficial electrochemistry of IrO_2/MoO_3 hybrid as a highly stable and efficient oxygen evolution reaction catalyst. ACS Sustain Chem Eng 6(4):4854–4862

[3] Tackett BM, Sheng W, Kattel S, Yao S, Yan B, Kuttiyiel KA, Chen JG (2018) Reducing iridium loading in oxygen evolution reaction electrocatalysts using core-shell particles with nitride cores. ACS Catal 8(3):2615–2621

[4] Reier T, Nong HN, Teschner D, Schlögl R, Strasser P (2017) Electrocatalytic oxygen evolution reaction in acidic environments—reaction mechanisms and catalysts. Adv Energy Mater 7(1):1601275

[5] Hu W, Wang Y, Hu X, Zhou Y, Chen S (2012) Three-dimensional ordered macroporous IrO_2 as electrocatalyst for oxygen evolution reaction in acidic medium. J Mater Chem 22(13):6010–6016

[6] Reier T, Oezaslan M, Strasser P (2012) Electrocatalytic oxygen evolution reaction (OER) on Ru, Ir, and pt catalysts: a comparative study of nanoparticles and bulk materials. ACS Catal 2(8):1765–1772

[7] Xu J, Aili D, Li Q, Christensen E, Jensen JO, Zhang W, Bjerrum NJ (2014) Oxygen evolution catalysts on supports with a 3-D ordered array structure and intrinsic proton

conductivity for proton exchange membrane steam electrolysis. Energy Environ Sci 7(2):820–830

[8] Hu W, Chen S, Xia Q (2014) IrO_2/Nb-TiO_2 electrocatalyst for oxygen evolution reaction in acidic medium. Int J Hydrogen Energy 39(13):6967–6976

[9] Tong J, Liu Y, Peng Q, Hu W, Wu Q (2017) An efficient Sb-SnO_2-supported IrO_2 electrocatalyst for the oxygen evolution reaction in acidic medium. J Mater Sci 52(23):13427–13443. Doi: https://doi.org/10.1007/s10853-017-1447-1

[10] Zhao S, Stocks A, Rasimick B, More K, Xu H (2018) Highly active, durable dispersed iridium nanocatalysts for PEM water electrolyzers. J Electrochem Soc 165(2):F82–F89

[11] Oh HS, Nong HN, Strasser P (2015) Preparation of mesoporous Sb-, F-, and In-doped SnO2 bulk powder with high surface area for use as catalyst supports in electrolytic cells. Adv Funct Mater 25(7):1074–1081

[12] Huang K, Li Y, Yan L, Xing Y (2014) Nanoscale conductive niobium oxides made through low temperature phase transformation for electrocatalyst support. RSC Adv 4(19):9701–9708

[13] Oh H-S, Nong HN, Reier T, Gliech M, Strasser P (2015) Oxide-supported Ir nanodendrites with high activity and durability for the oxygen evolution reaction in acid PEM water electrolyzers. Chem Sci 6(6):3321–3328

[14] Karimi F, Peppley BA (2017) Metal carbide and oxide supports for iridium-based oxygen evolution reaction electrocatalysts for polymer-electrolyte-membrane water electrolysis. Electrochim Acta 246:654–670

[15] Kuttiyiel KA, Sasaki K, Chen W, Su D, Adzic RR (2014) Core–shell, hollow-structured iridium–nickel nitride nanoparticles for the hydrogen evolution reaction. J Mater Chem A 2(3):591–594

[16] Rudenja S, Pan J, Wallinder IO, Leygraf C, Kulu P (1999) Passivation and anodic oxidation of duplex TiN coating on stainless steel. J Electrochem Soc 146(11):4082–4086

[17] Kakinuma K, Wakasugi Y, Uchida M, Kamino T, Uchida H, Watanabe M (2011) Electrochemical activity and durability of platinum catalysts supported on nanometer-size titanium nitride particles for polymer electrolyte fuel cells. Electrochemistry 79(5):399–403

[18] Yang S, Tak YJ, Kim J, Soon A, Lee H (2017) Support effect in single-atom platinum catalyst for electrochemical oxygen reduction support effect in single-atom platinum catalyst for electrochemical oxygen reduction. ACS Catal 7(2):1301–1307

[19] Zheng Y, Zhang J, Zhan H, Sun D, Dang D, Tian XL (2018) Porous and three dimensional titanium nitride supported platinum as an electrocatalyst for oxygen reduction reaction. Electrochem Commun 91:31–35

[20] Yang S, Kim J, Tak YJ, Soon A, Lee H (2016) Single-atom catalyst of platinum supported on titanium nitride for selective electrochemical reactions. Angew Chem Int Ed 55(6):2058–2062

[21] Li G, Li K, Yang L, Chang J, Ma R, Wu Z, Xing W (2018) Boosted performance of Ir species by employing TiN as the support toward oxygen evolution reaction. ACS Appl Mater Interfaces 10(44):38117–38124

[22] Cheng J, Zhang H, Ma H, Zhong H, Zou Y (2009) Preparation of $Ir_{0.4}Ru_{0.6}Mo_xO_y$ for oxygen evolution by modified Adams' fusion method. Int J Hydrogen Energy 34(16):6609–6661

[23] Ioroi T, Kitazawa N, Yasuda K, Yamamoto Y, Takenaka H (2000) Iridium oxide/platinum electrocatalysts for unitized regenerative polymer electrolyte fuel cells. J Electrochem Soc 147(6):2018–2022

[24] Ioroi T, Kitazawa N, Yasuda K, Yamamoto Y, Takenaka H (2001) IrO_2-deposited Pt electrocatalysts for unitized regenerative polymer electrolyte fuel cells. J Appl Electrochem 31(11):1179–1183

[25] Dong Y, Wu Y, Liu M, Li J (2013) Electrocatalysis on shape-controlled titanium nitride nanocrystals for the oxygen reduction reaction. ChemSusChem 6(10):2016–2021

[26] Wei Z, Wang Y, Zhang J (2018) Electrochemical detection of NGF using a reduced graphene oxide-titanium nitride nanocomposite. Sci Rep 8(1):6929

[27] Li C, Shi J, Zhu L, Zhao Y, Lu J, Xu L (2018) Titanium nitride hollow nanospheres with strong lithium polysulfide chemisorption as sulfur hosts for advanced lithium-sulfur batteries. Nano Res 11(8):4302–4312

[28] Liao Y, Xiang J, Yuan L, Hao Z, Gu J, Chen X, Huang Y (2018) Biomimetic root-like TiN/C@S nanofiber as a free-standing cathode with high sulfur loading for lithium-sulfur batteries. ACS Appl Mater Interfaces 10(44):37955–37962

[29] Yang C, Wang H, Lu S, Wu C, Liu Y, Tan Q, Xiang Y (2015) Titanium nitride as an electrocatalyst for V(II)/V(III) redox couples in all-vanadium redox flow batteries. Electrochim Acta 182:834–840

[30] Oktay S, Kahraman Z, Urgen M, Kazmanli K (2015) XPS investigations of tribolayers formed on TiN and (Ti, Re)N coatings. Appl Surf Sci 328:255–261

[31] Cui Z, Zu C, Zhou W, Manthiram A, Goodenough JB (2016) Mesoporous titanium nitride-enabled highly stable lithium-sulfur batteries. Adv Mater 28(32):6926–6931

[32] Zhao D, Cui Z, Wang S, Qin J, Cao M (2016) VN hollow spheres assembled from porous nanosheets for high-performance lithium storage and the oxygen reduction reaction. J Mater Chem A 4(20):7914–7923

[33] Pfeifer V, Jones TE, Velasco Vélez JJ, Massué C, Arrigo R, Teschner D, Hashagen M (2016) The electronic structure of iridium and its oxides. Surf Interface Anal 48(5):261–273

[34] Xiao H, Jia C, Liu B, Huang Y, Cai W, Li J, Huang Y (2019) Breaking long-range order in iridium oxide by alkali ion for efficient water oxidation. J Am Chem Soc 141(7):3014–3023

[35] Pfeifer V, Jones TE, Velasco Vélez JJ, Arrigo R, Piccinin S, Hävecker M, Schlögl R (2017) In situ observation of reactive oxygen species forming on oxygen-evolving iridium surfaces. Chem Sci 8(3):2143–2149

[36] Lee WH, Kim H (2011) Oxidized iridium nanodendrites as catalysts for oxygen evolution reactions. Catal Commun 12(6):408–411

[37] Kuo D-Y, Kawasaki JK, Nelson JN, Kloppenburg J, Hautier G, Shen KM, Suntivich J (2017) Influence of surface adsorption on the oxygen evolution reaction on IrO_2(110). J Am Chem Soc 139(9):3473–3479

[38] Mustain WE, Capuano CB, Maric R, Ayers KE, Zhao S, Danilovic N, Mustain WE (2015) Calculating the electrochemically active surface area of iridium oxide in operating proton exchange membrane electrolyzers. J Electrochem Soc 162(12):F1292–F1298

[39] Lettenmeier P, Wang L, Golla-Schindler U, Gazdzicki P, Cañas NA, Handl M, Friedrich KA (2016) Nanosized IrOx-Ir catalyst with relevant activity for anodes of proton exchange membrane electrolysis produced by a cost-effective procedure. Angew Chem Int Ed 55(2):742–746

[40] Hao C, Lv H, Mi C, Song Y, Ma J (2016) Investigation of mesoporous niobium-doped TiO_2 as an oxygen evolution catalyst support in an SPE water electrolyzer. ACS Sustain Chem Eng 4(3):746–756

[41] Han B, Risch M, Belden S, Lee S, Bayer D, Mutoro E, Yang SH (2018) Screening oxide support materials for OER catalysts in acid. J Electrochem Soc 165(10):F813–F820

[42] Rai S, Ikram A, Sahai S, Dass S, Shrivastav R, Satsangi VR (2017) CNT based photoelectrodes for PEC generation of hydrogen: a review. Int J Hydrogen Energy 42(7):3994–4006

[43] Guan J, Li D, Si R, Miao S, Zhang F, Li C (2017) Synthesis and demonstration of subnanometric iridium oxide as highly efficient and robust water oxidation catalyst. ACS Catal 7(9):5983–5986

[44] Zhou X, Yang J, Li C (2012) Theoretical study of structure, stability, and the hydrolysis reactions of small iridium oxide nanoclusters. J Phys Chem A 116(40):9985–9995

[45] Ping Y, Nielsen RJ, Goddard WA (2017) The reaction mechanism with free energy barriers at constant potentials for the oxygen evolution reaction at the IrO_2(110) surface. J Am Chem Soc 139(1):149–155

[46] Fuentes RE, Colon-Mercado HR, Martinez-Rodriguez MJ (2013) Pt-Ir/TiC electrocatalysts for PEM fuel cell/electrolyzer process. J Electrochem Soc 161(1):F77–F82

[47] Godínez-Salomón F, Albiter L, Alia SM, Pivovar BS, Camacho-Forero LE, Balbuena PB, Rhodes CP (2018) Self-supported hydrous iridium–nickel oxide two-dimensional nanoframes for high activity oxygen evolution electrocatalysts. ACS Catal 8(11):10498–10520

[48] Fu L, Zeng X, Cheng G, Luo W (2018) IrCo nanodendrite as an efficient bifunctional electrocatalyst for overall water splitting under acidic conditions. ACS Appl Mater Interfaces 10(30):24993–24998

[49] Jiang B, Wang T, Cheng Y, Liao F, Wu K, Shao M (2018) Ir/g-C_3N_4/nitrogen-doped graphene nanocomposites as bifunctional electrocatalysts for overall water splitting in acidic electrolytes. ACS Appl Mater Interfaces 10(45):39161–39167

[50] Nong HN, Oh HS, Reier T, Willinger E, Willinger MG, Petkov V, Strasser P (2015) Oxide-supported $IrNiO_x$ core-shell particles as efficient, cost-effective, and stable catalysts for electrochemical water splitting. Angew Chem Int Ed 54(10):297–2979

[51] Liang X, Shi L, Liu Y, Chen H, Si R, Yan W, Zou X (2019) Activating inert, nonprecious perovskites with iridium dopants for efficient oxygen evolution reaction under acidic conditions. Angew Chem Int Ed 58(23):7631–7635

[52] Frydendal R, Paoli EA, Knudsen BP, Wickman B, Malacrida P, Stephens IEL, Chorkendorff I (2014) Benchmarking the stability of oxygen evolution reaction catalysts: the importance of monitoring mass losses. ChemElectroChem 1:2075–2081